Check for updates

Novel Microstructural Features on Heat and Mass Transfer in Peristaltic Flow Through a Curved Channel

Raheel Ahmed[1†], Nasir Ali[1†], Sami Ullah Khan[2†], A. M. Rashad[3†], Hossam A. Nabwey[4,5†] and Iskander Tlili[6,7†]*

[1] Department of Mathematics and Statistics, International Islamic University Islamabad, Islamabad, Pakistan, [2] Department of Mathematics, COMSATS University Islamabad, Sahiwal, Pakistan, [3] Department of Mathematics, Faculty of Science, Aswan University, Aswan, Egypt, [4] Department of Mathematics, College of Science and Humanities in Al-Kharj, Prince Sattam bin Abdulaziz University, Al-Kharj, Saudi Arabia, [5] Department of Basic Engineering Science, Faculty of Engineering, Menoufia University, Shebin El-Kom, Egypt, [6] Department for Management of Science and Technology Development, Ton Duc Thang University, Ho Chi Minh City, Vietnam, [7] Faculty of Applied Sciences, Ton Duc Thang University, Ho Chi Minh City, Vietnam

Recently, significant interest has been developed by researchers toward the peristaltic transport of fluid, as this phenomenon involves a variety of applications in the biomechanics, bioengineering, and biomedical industries. In the present contribution, we investigate the effect of heat and mass transfer on magnetically influenced micropolar flow induced by peristaltic waves. The fundamental laws regarding current flow problem are employed by using curvilinear coordinates. A reduction of these equations is made based on lubrication approximation. The solution algorithm is based on the implementation of the famous finite difference method. The fundamental impacts of coupling number, micropolar parameter, Hartmann number, Brinkman number, rate of chemical reaction, and curvature parameter on longitudinal velocity, pressure rise, temperature, and mass concentration are analyzed in detail. The flow patterns in the channel illustrating the effects of several involved parameters are also displayed.

Keywords: micropolar fluid, hartmann number, heat and mass transfer, curved channel, implicit finite difference method

INTRODUCTION

The theory of fluids has gained the attention of scientists, engineers, biologists, and mathematicians in recent times. Generally, fluids are categorized as Newtonian or non-Newtonian. Newtonian fluids are those in which viscous stresses sustain a linear relationship between strain rates at every point. The viscous fluids are referred to as a simple linear model that reports the viscosity. Examples of Newtonian fluids are water, glycerol, alcohol, thin motor oil, and air. Another class of fluids is defined as a fluid which fails to follow Newton's viscosity model. A number of fluids are non-Newtonian in nature. Examples are custard, ketchup, shampoo, starch, paint, blood, and suspension. Recently, many researchers have been concentrating on the flows of non-Newtonian fluids. This is due to the applications of non-Newtonian fluids in polymer processing, biofluid mechanics, and complex mathematical non-linear constitutive equations.

The motivating implication of the Peristalsis phenomenon has attained a valuable attraction of scientists in the last few years as it involves fundamental industrial and bioscience applications. Several investigations are reported regarding the peristaltic transport of non-Newtonian materials which encountered many physiology applications. Raju and Devanathan [1] worked on the peristaltic study of the power law model configured by a tube, where it was assumed that a sinusoidal with lower amplitude traveled down along the channel wall. Mekheimer [2] studied the transport of magnetohydrodynamic viscous and incompressible peristaltic flow in an inclined planar channel. Hakeem et al. [3] modeled the peristaltic flow motion equations for Carreau fluid by using long wavelength assumptions in a uniform tube. The peristaltic study of Johnson–Segalman liquid influenced by magnetic force in a 2D flexible channel has been depicted by Elshahed and Haroun [4]. Hakeem et al. [5] examined the significance of magnetic force in trapping evolved regarding the peristaltic flow generalized viscous fluid. The rheological justification of non-Newtonian Burger's fluid due to peristaltic movement encountered by a planar channel was reported by Hayat et al. [6]. The reported flow model was based on long wavelength theory, and later on, an exact solution is developed for a formulated problem. The theoretical model developed by Haroun [7] signified the rheological consequences in third-order liquid for a peristaltic phenomenon configured by the asymmetric channel. Wang et al. [8] studied the magnetohydrodynamic peristaltic motion of a Sisko fluid in a symmetric or asymmetric channel. An investigation with peristaltic aspects for third-grade fluid encountered by a circular cylindrical tube was performed by Ali et al. [9]. The peristaltic mechanism of Prandtl–Eyring fluid along with heat transfer features in a curved channel was evaluated by Hayat et al. [10]. Rafiq et al. [11] investigated ion-slip and Hall features in the peristaltic flow of nanoparticles with biomedical applications. Ahmed and Javed [12] used finite element technique to model Navier–Stokes expressions for the peristaltic phenomenon in the presence of a porous medium. The influence of electromagnetic features in the peristaltic flow of Eyring-Powell nanofluid. Asha

and Sunitha [13] involved the Hall effects in peristaltic transport of nanoparticles in the asymmetric channel.

Non-Newtonian fluids are characterized through a number of models due to their complexity. Among these models, a micropolar fluid model has been gaining attention of a number of researchers. In this model, stiff particles cramped into a relatively minute-volume element are able to move about the center of the element. The rotational attribute of fluid particles is carried out through a vector called micro-rotation expressions. It is not worth remarking that those intrinsic rotation features of the fluid are associated with rigid body movement for a whole-volume element which depends upon various factors. Such features are referred to the micro-rotational effects, and the role of these factors at macro-scale cannot be taken into account. However, such effects become important when flow is considered in narrow gaps, i.e., when geometric dimensions of the flow domain are very small [14]. In peristaltic flows, fluid is usually pushed through nano-size vessels, and therefore, it is expected that micro-rotation of particles reflects some diverse and distinguished flow characteristics. Important effects cannot be captured by the Navier–Stokes theory. The fundamental work on the micropolar fluid theory was first introduced by Eringen [15, 16] to describe the suspensions of neutrally buoyant rigid particles in a viscous fluid. The work on micropolar fluid was initiated by Eringen by involving the micro-rotation features in the classical Navier–Stokes theory. Ariman et al. [17] studied the application of micro-continuum fluid mechanics in a broader prospect. The assessment of a boundary layer for the micropolar fluid has been successfully examined by Na and Pop [18]. Srinivasacharya et al. [19] reported a closed-form relation for peristaltic aspects of micropolar fluid flow due to a circular tube. The model problem was based on the famous long wavelength and small Reynolds number assumptions. The peristaltic movement under the influence of wall properties in 2D flow of micropolar liquid has been revealed by Muthu et al. [20]. Lok et al. [21] investigated the steady mixed convective due to vertical moving geometry for flow of micropolar fluid. Hayat et al. [22] examined the impact of different waveforms in a peristaltic flow of a micropolar fluid. The flow of micropolar liquid followed by a peristaltic pattern in the asymmetric channel has been focused by Ali and Hayat [23]. Another continuation made by Hayat and Ali [24] reported the endoscope consequences for micropolar fluid flow in a concentric tube. Another peristaltic phenomenon based on an exploration for micropolar liquid with implementation of magnetic field impact was estimated by Mekheimer [25]. Ishak et al. [26] studied the magnetohydrodynamic flow of a micropolar fluid toward a stagnation point on a vertical surface. Mekheimer and El Kot [27] used the micropolar fluid model for blood flow through a stenosed tapered artery. Sajid et al. [28] employed the homotopy analysis method to discuss boundary layer flow micropolar fluid through a porous channel. Ashraf et al. [29] examined numerical solutions portraying the appliance of micropolar material in a channel having porous walls. Rashidi et al. [30] applied the differential transform method to get a semi-analytical solution of micropolar flow in a porous channel with mass injection. Ali et al. [31] comprehensively studied the peristaltic flow of a micropolar fluid in a curved channel. The unsteady peristaltic prospective
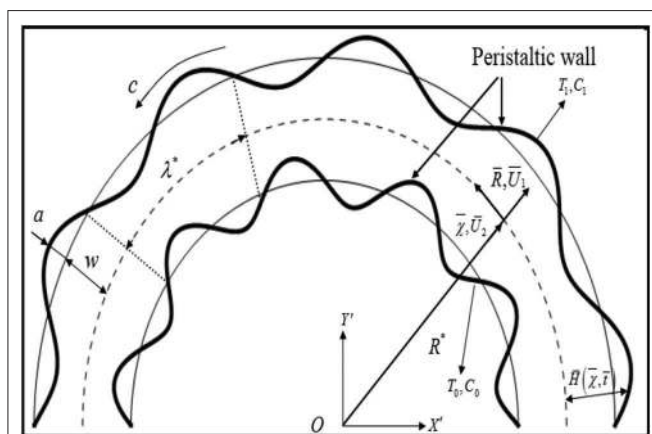

FIGURE 1 | Physical problem of the peristaltic flow regime.

for 2D channel flow of micropolar fluid in the presence of heat and mass transportation has been examined by El-Dabe and Zeid [32]. The investigation for micropolar fluid in contacting a wall channel additionally featuring an isotropic porous space was assessed by Abd Elmaboud [33]. Sui et al. [34] reported a constitutive diffusion model to investigate the heat transfer performances in micropolar fluid encountered by a moving geometry. Waqas et al. [35] numerically predicted the join
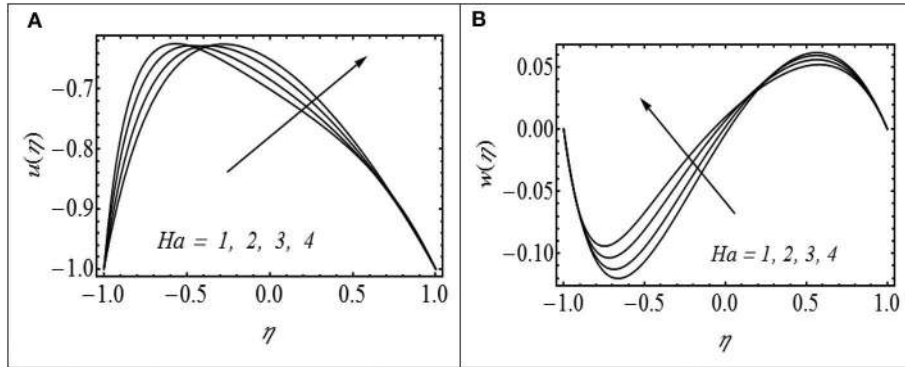
FIGURE 2 | (A,B) Impact of Ha on $u(\eta)$ with $\gamma = 2.5$, $N_1 = 0.5$, $N_2 = 1.2$, $\lambda = 0.4$, and $\Theta = 1.5$. (B) Impact of Ha on $w(\eta)$ with $\gamma = 2.5$, $N_1 = 0.5$, $N_2 = 1.2$, $\lambda = 0.4$, and $\Theta = 1.5$.
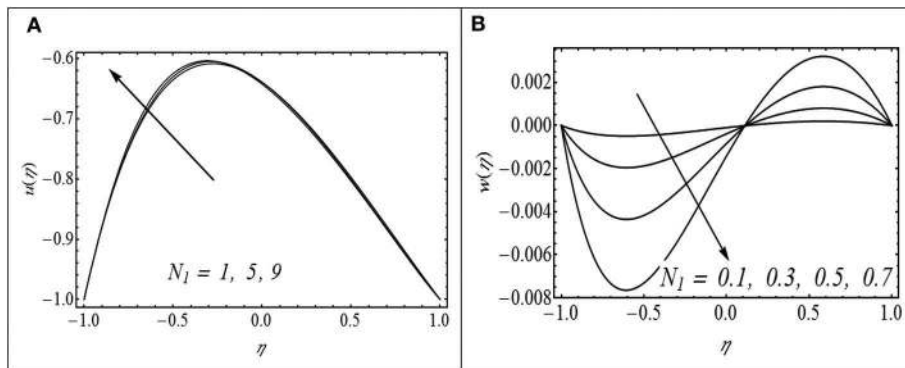
FIGURE 3 | (A,B) Impact of N_1 on $u(\eta)$ with $\gamma = 2.5$, $Ha = 2$, $N_2 = 0.2$, $\lambda = 0.4$, and $\Theta = 1.5$. (B) Impact of N_1 on $w(\eta)$ with $\gamma = 2.5$, $N_2 = 0.2$, $\lambda = 0.4$, and $\Theta = 1.5$.
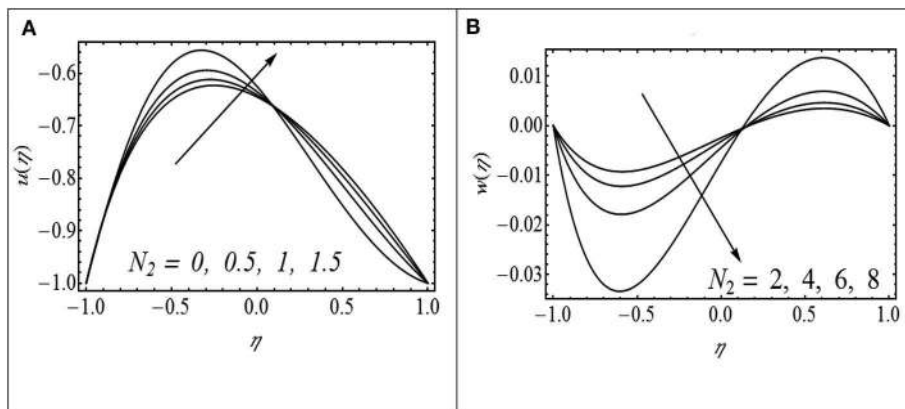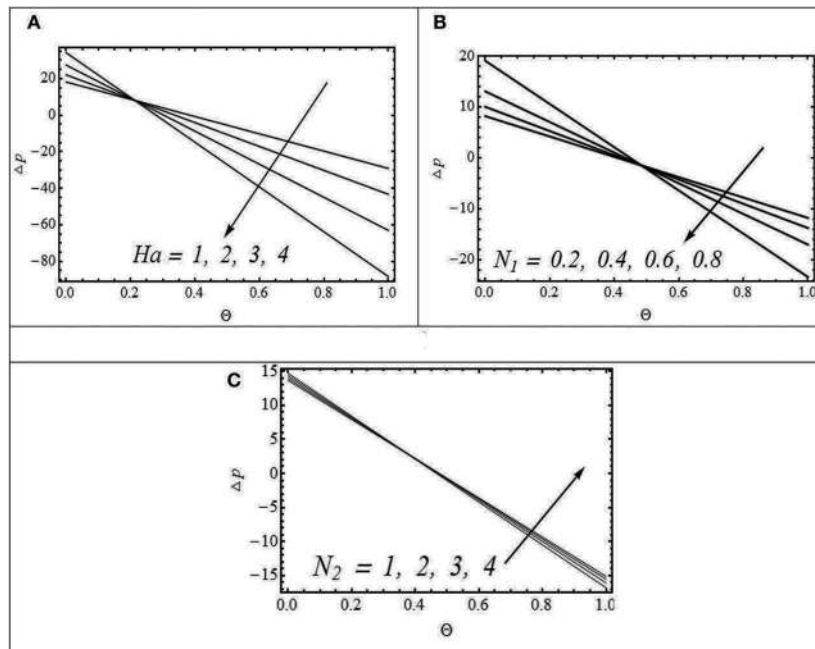

FIGURE 4 | (A,B) Impact of N_2 on $u(\eta)$ with $\gamma = 2.5$, $Ha = 2$, $N_1 = 0.5$, $\lambda = 0.4$, and $\Theta = 1.5$. (B) Impact of N_2 on $w(\eta)$ with $\gamma = 2.5$, $N_1 = 0.5$, $\lambda = 0.4$, and $\Theta = 1.5$.

features of Maxwell viscoelasticity–based nanofluid additionally featuring a porous medium. In another contribution, Waqas and co-workers [36] utilized the bioconvection phenomenon in the flow of micropolar nanofluid with additional thermal radiation features. Ali et al. [37] intended the micropolar liquid rheological significance compiled in calendaring geometry. Ahmed et al. [38] examined the effects of heat and mass transfer on peristaltic flow of Sisko fluid through a curved channel. Mekheimer et al.

FIGURE 5 | (A) Impact of Ha on Δp with $N_1 = 0.5, N_2 = 1.2$, $\gamma = 2.5$, and $\lambda = 0.4$. (B) Impact of N_1 on Δp with $\gamma = 2.5$, $N_2 = 1.2$, and $\lambda = 0.4$. (C) Impact of N_2 on Δp with $N_1 = 0.5$, $\gamma = 2.5$, and $\lambda = 0.4$.
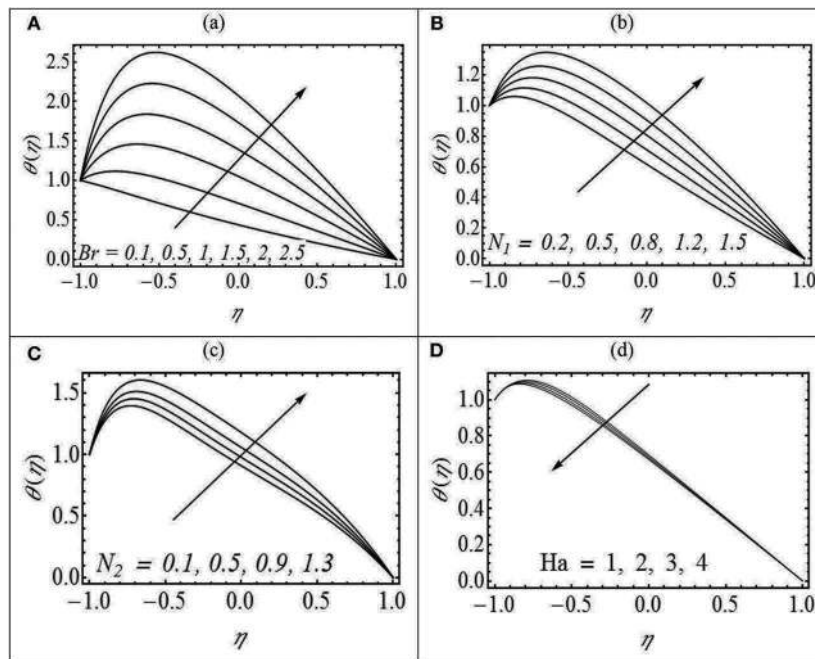
FIGURE 6 | (A–D) Variation in θ for various values of (A) Br with $N_1 = 0.5$, $N_2 = 1.2$, $\lambda = 0.4$, and $\gamma = 2$; (B) N_1 with $Br = 2$, $N_2 = 1.2$, $\lambda = 0.4$, and $\gamma = 2$; (C) N_2 with $Br = 2$, $N_1 = 0.5$, $\lambda = 0.4$, and $\gamma = 2$; and (D) Ha with $N_1 = 0.5$, $N_2 = 1.2$, $\lambda = 0.4$, and $\gamma = 2$.

[39] studied the effect of gold nanoparticle third-grade fluid on peristaltic blood flow. Elkhair et al. [40] considered the impact of heat transfer on oscillatory flow of a dielectric fluid through a porous medium. Recently, Mekheimer et al. [41] investigated the behavior of a blood confined by stenotic arterial walls. In another useful attempt, Mekheimer et al. [42] performed the features of heat transfer additionally featuring AC current. Nadeem et al. [43, 44] studied hybrid-based nanofluid flow over a curved surface in different scenarios. Abbas et al. [45] observed transportation of micropolar hybrid nanomaterial which was externally impacted by magnetic influence. Sadaf et al. [46] discussed the effect of heat transfer on fluid motion generated by cilia and a pressure gradient in a curved channel. In a most recent study, Nadeem et al. [47] investigated the effect of heat transfer on micropolar fluid flow over a Riga plate. Some more recent investigations on this topic are seen in references [48–50].

From the literature cited above, it is noted that the hydrodynamic flow of micropolar fluid through a curved channel with peristalsis is studied but less attention is paid to hydromagnetic aspects of micropolar liquid along with heat and mass transportation aspects. The prime objective of this study is to investigate the effects of coupling number, micropolar parameter, Hartmann number, Brinkman number, and dimensionless radius of curvature on flow, heat, and mass transfer characteristics. To this end, the associated equations for velocity, temperature, and mass concentration are constituted. The modeled system is numerically interpolated with assistance

of finite difference scheme. The fluid velocity, temperature, and concentration fields are analyzed for several values of the involved parameters. It is important to mention that governing equations for heat and mass transfer for the flow of micropolar fluid in a curved peristaltic channel are derived for the first time in the literature.

GOVERNING EQUATIONS

For micropolar fluid, the mathematical expressions in presence of heat/mass influences are given by [37].

Continuity equation:

$$U_{i,i} = 0 \tag{1}$$

Momentum equation:

$$\rho \dot{U}_k = \tau_{lk,l} + \rho f_k \tag{2}$$

Moment of momentum equation:

$$\rho j \dot{w}_k = m_{lk,l} + e_{kij} \tau_{ij} \tag{3}$$

Energy equation:

$$\rho c_p \dot{T} = k T_{,ii} + \tau_{kl} a_{kl} - m_{kl} b_{kl} \tag{4}$$
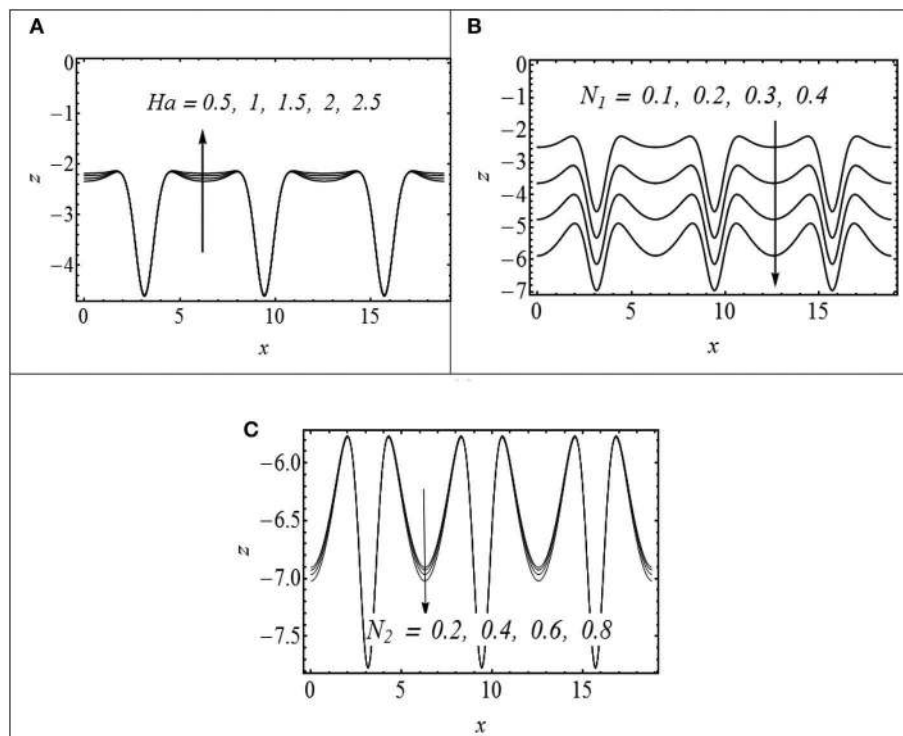
FIGURE 7 | (A–C) Variation in z at the upper wall for **(A)** Ha with $N_1 = 0.5$, $N_2 = 1.2$, $\lambda = 0.4$, and $\gamma = 2$; **(B)** N_1 with $Br = 2$, $N_2 = 1.2$, $\lambda = 0.4$, and $\gamma = 2$; and **(C)** N_2 with $Br = 2$, $N_1 = 0.5$, $\lambda = 0.4$, and $\gamma = 2$.

Concentration equation:

$$\dot{C} = DC_{,ii} + \frac{Dk_T}{T_m} T_{,ii} - k_1 C \qquad (5)$$

In the above equations, U_k is the velocity, C is the mass concentration, f_k is the body force, T is the symbolized temperature, τ_{kl} is the Cauchy stress tensor, m_{kl} is the moment stress tensor, p is the pressure, ρ is the fluid density, w_k is the micro-rotation vector, c_p is the specific heat at constant pressure, D is the coefficient of mass diffusivity, K_T is the thermal diffusivity, T_m is the mean temperature, k_1 is the rate of chemical reaction, k is the thermal conductivity, j is the micro moment of inertia, and dot indicates the material time derivative. Moreover, $\tau_{kl}, m_{kl}, a_{kl}$ and b_{kl} are given by

$$\left.\begin{array}{l} \tau_{kl} = -p\delta_{kl} + (\mu + k_2) a_{kl} + \mu a_{lk}, \\ m_{kl} = \alpha\, tr(b_{mm})\delta_{kl} + \beta b_{kl} + \gamma^* b_{lk}, \\ a_{kl} = v_{l,k} + e_{lkm}w_m, \\ b_{kl} = w_{k,l}, \end{array}\right\} \qquad (6)$$

where μ is the viscosity, k_2 is the dynamic micro-rotation viscosity, e_{lkm} is the permutation symbol, and α, β, γ^* are the constants called coefficient of angular viscosity. It is remarked that Equation (2) has been diminished into a Navier–Stokes expression when $k_2 = \alpha = \beta = \gamma^* = 0$. It is further emphasized that if $k_2 = 0$, both micro-rotation and velocity are unyoked and micro-rotation does not play to alter the global motion. Following Eringen [51], the following relations hold for $\mu, k_2, \alpha, \beta,$ and γ^*

$$2\mu + k_2 \geq 0, k_2 \geq 0, 3\alpha + \beta + \gamma^* \geq 0, \alpha \geq |\beta|.$$

MATHEMATICAL MODELING

Consider a curved channel of width $2w$ coiled in circle having radius R_0 and center O. An incompressible micropolar fluid flows inside the channel. The fluid flows due to the wall of the channel which deforms uniformly. Let $T_0, T_1, C_0,$ and C_1 represent the upper wall temperature, lower wall temperature, upper
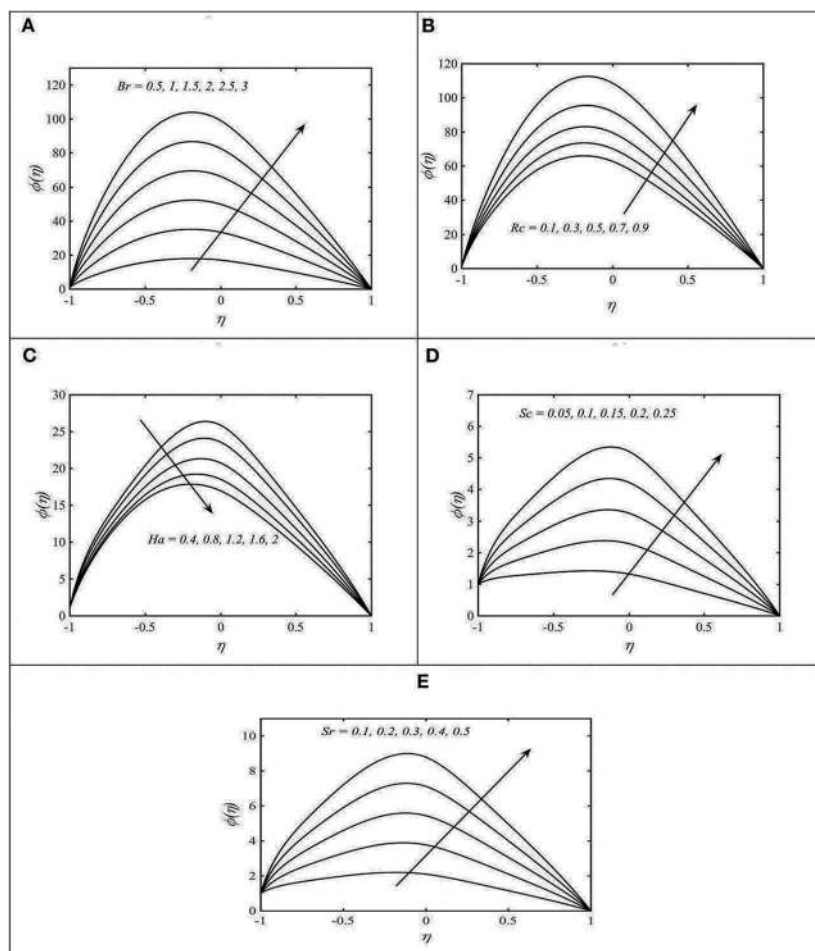
FIGURE 8 | (A–D) Change in φ for various values of **(A)** Br with $N_1 = 0.5$, $N_2 = 1.2$, $\lambda = 0.4$, and $\gamma = 2$; **(B)** R_c with $Br = 2$, $N_1 = 0.5$, $N_2 = 1.2$, $\lambda = 0.4$, and $\gamma = 2$; **(C)** Ha with $Br = 2$, $N_1 = 0.5$, $N_2 = 1.2$, $\lambda = 0.4$, and $\gamma = 2$; **(D)** Sc with $Br = 2$, $N_1 = 0.5$, $N_2 = 1.2$, $\lambda = 0.4$, and $\gamma = 2$; and **(E)** Sr with $Br = 2, N_1 = 0.5$, $N_2 = 1.2, \lambda = 0.4$, and $\gamma = 2$.

wall concentration, and lower wall concentration, respectively. The fluid movement is described by following the curvilinear coordinate system (R, χ, Z). It is emphasized that χ is specified in the flow direction and R is radially oriented while Z is assumed normal to the plane. The flow visualization for the current problem can be described by sketching **Figure 1**. The shape of both walls is described mathematically as [31, 38]

$$H_1(\chi, t) = w + a \sin\left(\left(\frac{2\pi}{\lambda^*}\right)(\chi - ct)\right), \quad \text{Upper wall, (7)}$$

$$H_2(\chi, t) = -w - a\sin\left(\left(\frac{2\pi}{\lambda^*}\right)(\chi - ct)\right), \quad \text{Lower wall, (8)}$$

where λ^* is the wavelength, c is the wave speed, a is the amplitude, and t is the time. The present work is based on the following assumptions:

where B^* is the limiting value of B when $\tilde{R} \rightarrow \infty$. Thus, by generalizing Ohm's law, the body force term in Equation (2) becomes

$$\rho f_k = (\mathbf{J} \times B)_{\mathbf{k}},$$

where $J = \sigma(V \times B)$. Here, we neglect the electric field and invoke the low magnetic Reynolds number assumption. Using the velocity, temperature, concentration, and micro-rotation fields defined by

$$\mathbf{U} = [U_1(\chi, R, t), U_2(\chi, R, t), 0], \quad T = T(\chi, R, t),$$
$$C = C(\chi, R, t), \mathbf{w} = [0, 0, -w(x, r)]$$

the set of Equations (1)–(5) in component form becomes [31, 38]

$$\frac{\partial}{\partial R}\{(R + \tilde{R})U_1\} + \tilde{R}\frac{\partial U_2}{\partial \chi} = 0, \tag{9}$$

$$\frac{\partial U_1}{\partial t} + (U_1.\nabla)U_1 - \frac{U_2^2}{R + \tilde{R}} = -\frac{1}{\rho}\frac{\partial P}{\partial R} + \frac{1}{\rho}(\mu + k_2)\left[\nabla^2 U_1 - \frac{U_1}{(R + \tilde{R})^2} - \frac{2\tilde{R}}{(R + \tilde{R})^2}\frac{\partial U_2}{\partial \chi}\right] + \frac{k_2\tilde{R}}{\rho(R + \tilde{R})}\frac{\partial w}{\partial \chi}, \tag{10}$$

$$\frac{\partial U_2}{\partial t} + (U_1.\nabla)U_2 + \frac{U_1 U_2}{R + \tilde{R}} = -\frac{\tilde{R}}{\rho(R + \tilde{R})}\frac{\partial P}{\partial \chi} + \frac{1}{\rho}(\mu + k_2)\left[\nabla^2 U_2 - \frac{U_2}{(R + \tilde{R})^2} + \frac{2\tilde{R}}{(R + \tilde{R})^2}\frac{\partial U_1}{\partial \chi}\right] - \frac{k_2}{\rho}\frac{\partial w}{\partial R} - \frac{\sigma B^{*2}\tilde{R}^2}{\rho(R + \tilde{R})^2}U_2, \tag{11}$$

$$(U_1.\nabla)w = -\frac{\gamma^*}{\rho j}\left[\frac{\partial^2 w}{\partial R^2} + \frac{1}{R + \tilde{R}}\frac{\partial w}{\partial R} + \left(\frac{\tilde{R}}{R + \tilde{R}}\right)^2\frac{\partial^2 w}{\partial \chi^2}\right] + \frac{k_2}{\rho j}\left[2w - \frac{\tilde{R}}{R + \tilde{R}}\frac{\partial U_1}{\partial \chi} + \frac{\partial U_2}{\partial R} + \frac{U_2}{R + \tilde{R}}\right], \tag{12}$$

$$\rho c_p\left(\frac{\partial T}{\partial t} + U_1\frac{\partial T}{\partial R} + \frac{U_2\tilde{R}}{R + \tilde{R}}\frac{\partial T}{\partial \chi}\right) = k\left(\frac{\partial^2 T}{\partial R^2} + \frac{1}{R + \tilde{R}}\frac{\partial T}{\partial R} + \frac{\tilde{R}^2}{(R + \tilde{R})^2}\frac{\partial^2 T}{\partial \chi^2}\right) + \frac{\partial U_1}{\partial R}\left(-p + 2\mu\frac{\partial U_1}{\partial R} + k_2\frac{\partial U_1}{\partial R}\right)$$

$$+ \left(\frac{\tilde{R}}{R + \tilde{R}}\frac{\partial U_1}{\partial \chi} - \frac{U_2}{R + \tilde{R}} - w\right)\left(\frac{\mu\tilde{R}}{R + \tilde{R}}\frac{\partial U_1}{\partial \chi} + \mu\frac{\partial U_2}{\partial R} - \frac{\mu U_2}{R + \tilde{R}} + \frac{k\tilde{R}}{R + \tilde{R}}\frac{\partial U_1}{\partial \chi} - \frac{kU_2}{R + \tilde{R}} - k_2 w\right)\left(\frac{\partial U_2}{\partial R} + w\right)$$

$$\left(\frac{\mu\tilde{R}}{R + \tilde{R}}\frac{\partial U_1}{\partial \chi} + \mu\frac{\partial U_2}{\partial R} - \frac{\mu U_2}{R + \tilde{R}} + k_2\frac{\partial U_2}{\partial R} + k_2 w\right) + \left(\frac{\tilde{R}}{R + \tilde{R}}\frac{\partial U_2}{\partial \chi} + \frac{U_1}{R + \tilde{R}}\right)\left(-p + \frac{2\mu\tilde{R}}{R + \tilde{R}}\frac{\partial U_2}{\partial \chi} + \frac{2\mu U_1}{R + \tilde{R}} + \frac{k\tilde{R}}{R + \tilde{R}}\frac{\partial U_2}{\partial \chi} + \frac{kU_1}{R + \tilde{R}}\right)$$

$$+ \gamma^*\left(\left(\frac{\partial w}{\partial R}\right)^2 + \left(\frac{\tilde{R}}{R + \tilde{R}}\frac{\partial w}{\partial \chi}\right)^2\right), \tag{13}$$

$$\frac{\partial C}{\partial t} + (U_1.\nabla)C = D\nabla^2 C + \frac{DK_T}{T_m}\left(\frac{\partial^2 T}{\partial R^2} + \frac{\tilde{R}}{R + \tilde{R}}\frac{\partial T}{\partial R} + \left(\frac{\tilde{R}}{R + \tilde{R}}\right)^2\frac{\partial^2 T}{\partial \chi^2}\right) - k_1 C, \tag{14}$$

(1) The fluid is assumed as a continuum.
(2) Fluid is incompressible.
(3) The solid matrix is in a local thermal equilibrium with the fluid.
(4) The walls of the channel are non-compliant.
(5) Flow is laminar with negligible gravitational effects.
(6) The magnetic Reynolds number is assumed small, and hence, effects of induced magnetic field are negligible.
(7) Soret and chemical effects are taken into account.

It is further assumed that the flow is subjected to the radial magnetic field of the form

$$\mathbf{B} = \left(\frac{B^*\tilde{R}}{R + \tilde{R}}\right)\mathbf{e}_R,$$

where

$$U_1.\nabla = U_1\frac{\partial}{\partial R} + \frac{\tilde{R}U_2}{R + \tilde{R}}\frac{\partial}{\partial \chi}, \tag{15}$$

and

$$\nabla^2 = \frac{1}{R + \tilde{R}}\frac{\partial}{\partial R}\left\{(R + \tilde{R})\frac{\partial}{\partial R}\right\} + \left(\frac{\tilde{R}}{R + \tilde{R}}\right)^2\frac{\partial^2}{\partial \chi^2} \tag{16}$$

The boundary conditions associated with Equations (9)–(14) are [8]

$$U_2 = 0, U_1 = \frac{\partial H_1}{\partial t}, w = 0, T = T_o, C = C_o \text{ at } R = H_1(\chi, t), \tag{17}$$

$$U_2 = 0, U_1 = \frac{\partial H_2}{\partial t}, w = 0, T = T_1, C = C_1 \text{ at } R = H_2(\chi, t). \tag{18}$$

The following transformations are suggested to transmute the fixed wave from (R, χ) to new wave from (r, x)

$$x = \chi - ct, \quad r = R, \quad p = P, \quad u_1 = U_1, \quad u_2 = U_2 - c. \quad (19)$$

The governing flow equation is transmuted into a wave frame while defining the following appropriate variables [31, 38]:

$$\bar{x} = \frac{2\pi x}{\lambda^*}, \quad \eta = \frac{r}{a}, \quad \gamma = \frac{\tilde{R}}{a}, \quad \bar{u}_1 = \frac{u_1}{c}, \quad \bar{u}_2 = \frac{u_2}{c},$$

$$\bar{w} = \frac{aw}{c}, \quad \bar{p} = \frac{2\pi a^2 p}{\lambda^* \mu c}, \quad \mathrm{Re} = \frac{\rho ca}{\mu}, \quad \theta = \frac{(T-T_1)}{(T_0-T_1)},$$

$$\phi = \frac{(C-C_1)}{(C_0-C_1)}, \quad \delta = \frac{2\pi a}{\lambda^*}, \quad \bar{j} = \frac{j}{a^2}, \quad N_1 = \frac{k^2}{\mu}, \quad N_2 = \frac{\gamma^*}{a^2 \mu}$$

Moreover, invoking the lubrication approximations ($\delta \approx 0$, $\mathrm{Re} \approx 0$) reduces to

$$\frac{\partial p}{\partial \eta} = 0, \qquad (20)$$

$$-\frac{\partial p}{\partial x} - \frac{1}{\gamma(1-N_1)}\left[\frac{\partial}{\partial \eta}\left\{ (\eta+\gamma)\frac{\partial^2 \psi}{\partial \eta^2} \right\} + \frac{1}{\eta+\gamma}\left(1-\frac{\partial \psi}{\partial \eta}\right) - N_1(\eta+\gamma)\frac{\partial w}{\partial \eta} \right] - \frac{\gamma Ha^2}{\eta+\gamma}\left(1-\frac{\partial \psi}{\partial \eta}\right) = 0, \qquad (21)$$

$$\left(\frac{2-N_1}{N_2}\right)\left[\frac{\partial^2 w}{\partial \eta^2} + \frac{1}{\eta+\gamma}\frac{\partial w}{\partial \eta}\right] - 2w + \frac{\partial^2 \psi}{\partial \eta^2} - \frac{1}{\eta+\gamma}\left(1-\frac{\partial \psi}{\partial \eta}\right) = 0, \qquad (22)$$

$$\frac{\partial^2 \theta}{\partial \eta^2} + \frac{1}{(\eta+\gamma)}\frac{\partial \theta}{\partial \eta} + Br\left(\frac{1}{\eta+\gamma}\left(1-\frac{\partial \psi}{\partial \eta}\right) + w\right)$$
$$\left(\frac{\partial^2 \psi}{\partial \eta^2} + \frac{1}{\eta+\gamma}\left(1-\frac{\partial \psi}{\partial \eta}\right)(1+N_1) + N_1 w\right) + \qquad (23)$$
$$Br\left(\frac{\partial^2 \psi}{\partial \eta^2} - w\right)\left(\frac{\partial^2 \psi}{\partial \eta^2} + \frac{1}{\eta+\gamma}\left(1-\frac{\partial \psi}{\partial \eta}\right) + N_1\left(\frac{\partial^2 \psi}{\partial \eta^2} - w\right)\right) + N_2 Br\left(\frac{\partial w}{\partial \eta}\right)^2 = 0,$$

$$\frac{\partial^2 \phi}{\partial \eta^2} + \frac{1}{(\eta+\gamma)}\frac{\partial \phi}{\partial \eta} - R_c \phi = -SrSc\left(\frac{\partial^2 \theta}{\partial \eta^2} + \frac{1}{(\eta+\gamma)}\frac{\partial \theta}{\partial \eta}\right) + R_c. \qquad (24)$$

In the above equations N_1, N_2, Re, δ, γ, K^*, and R_c represent the coupling number, micropolar constant, Reynolds number, wave number, radius of curvature, dimensionless permeability parameter, and dimensionless rate of the chemical reaction parameter, respectively. Here, the coupling number presents the coupling between the vortex viscosity and shear viscosity coefficients, while micropolar parameter is the ratio between the coefficient of angular viscosity and the shear viscosity coefficient. Further, the stream function ψ and velocity components u_1 and u_2 are related through the expressions

$$u_1 = \delta \frac{\gamma}{\eta+\gamma}\frac{\partial \psi}{\partial x}, \quad u_2 = -\frac{\partial \psi}{\partial \eta}. \qquad (25)$$

Combining Equation (20) with Equation (21), one gets

$$\frac{1}{1-N_1}\left[\frac{\partial^2}{\partial \eta^2}\left\{(\eta+\gamma)\frac{\partial^2 \psi}{\partial \eta^2}\right\} + \frac{\partial}{\partial \eta}\left(\frac{1}{\eta+\gamma}\left(1-\frac{\partial \psi}{\partial \eta}\right)\right) - N_1\frac{\partial}{\partial \eta} \right.$$
$$\left. \left((\eta+\gamma)\frac{\partial w}{\partial \eta}\right)\right] - \frac{\gamma^2 Ha^2}{\eta+\gamma}\left(1-\frac{\partial \psi}{\partial \eta}\right) = 0. \qquad (26)$$

The transmuted boundary assumptions (17)–(18) are

$$\psi = -\frac{q}{2}, \quad \frac{\partial \psi}{\partial \eta} = 1, \quad w = 0, \theta = 0, \quad \phi = 0, \text{ at}$$
$$\eta = h_1 = 1 + \lambda \sin x, \qquad (27)$$

$$\psi = \frac{q}{2}, \quad \frac{\partial \psi}{\partial \eta} = 1, \quad w = 0, \quad \theta = 1, \quad \phi = 1, \text{ at}$$
$$\eta = h_2 = -1 - \lambda \sin x. \qquad (28)$$

In the above set of equations, $\lambda = \frac{a}{w}$ symbolizes the amplitude ratio. Our objective is to compute the solution of Equations (22)–(24) and (26) subject to boundary conditions (27) and (28).

We summarized the following relations for pressure rise per wavelength (Δp), heat transfer coefficients $z_i(i = 1, 2)$, and expressions for Sherwood number $Sh_i(i = 1, 2)$ at the upper and lower wall surfaces in the following forms:

$$\Delta p = \int_0^{2\pi} \frac{dp}{dx}dx, \qquad (29)$$

$$z_i = \left.\frac{\partial h_i}{\partial x}\frac{\partial \theta}{\partial \eta}\right|_{\eta = h_i}, \quad i = 1, 2. \qquad (30)$$

$$Sh = \left.\frac{\partial h_i}{\partial x}\frac{\partial \phi}{\partial \eta}\right|_{\eta = h_i}. \quad i = 1, 2. \qquad (31)$$

NUMERICAL SOLUTION

In this, we numerically address the solution procedure of Equations (27), (28), and (30) subject to boundary conditions given in Equations (31) and (32). On this end, we adopted a famous finite difference procedure to perform such numerical simulations [52–54]. According to this method, simulations are performed by the following steps:

(i) As a first step, an iterative procedure has been compiled by transmuting non-linear flow equations into linear equations at the $(m + 1)$th iterative step. Adopting such iterative process, we get

$$\frac{\partial^4 \psi^{(m+1)}}{\partial \eta^4} + \frac{2}{(\eta + \gamma)} \frac{\partial^3 \psi^{(m+1)}}{\partial \eta^3} - \frac{1}{(\eta + \gamma)^2} \frac{\partial^2 \psi^{(m+1)}}{\partial \eta^2} + \left\{ \frac{1}{(\eta + \gamma)^3} + \frac{\gamma^2 Ha^2 (1 - N_1)}{(\eta + \gamma)^2} \right\} \frac{\partial \psi^{(m+1)}}{\partial \eta}$$

$$- N_1 \frac{\partial^2 w^{(m+1)}}{\partial \eta^2} - \frac{N_1}{(\eta + \gamma)} \frac{\partial w^{(m+1)}}{\partial \eta} - \frac{1}{(\eta + \gamma)^3} - \frac{\gamma^2 Ha^2 (1 - N_1)}{(\eta + \gamma)^2} = 0. \tag{32}$$

$$\frac{\partial^2 \theta^{(m+1)}}{\partial \eta^2} + \frac{1}{(\eta + \gamma)} \frac{\partial \theta^{(m+1)}}{\partial \eta} + Br \left(\frac{1}{\eta + \gamma} \left(1 - \frac{\partial \psi^{(m)}}{\partial \eta} \right) + w^{(m)} \right) \left(\frac{\partial^2 \psi^{(m)}}{\partial \eta^2} + \frac{1}{\eta + \gamma} \left(1 - \frac{\partial \psi^{(m)}}{\partial \eta} \right) (1 + N_1) + N_1 w^{(m)} \right) +$$

$$Br \left(\frac{\partial^2 \psi^{(m)}}{\partial \eta^2} - w^{(m)} \right) \left(\frac{\partial^2 \psi^{(m)}}{\partial \eta^2} + \frac{1}{\eta + \gamma} \left(1 - \frac{\partial \psi^{(m)}}{\partial \eta} \right) + N_1 \left(\frac{\partial^2 \psi^{(m)}}{\partial \eta^2} - w^{(m)} \right) \right) + N_2 Br \left(\frac{\partial w^{(m)}}{\partial \eta} \right)^2 = 0, \tag{33}$$

$$\frac{\partial^2 \phi^{(m+1)}}{\partial \eta^2} + \frac{1}{\eta + \gamma} \frac{\partial \phi^{(m+1)}}{\partial \eta} - R_c \phi^{(m+1)} = -SrSc \left(\frac{\partial^2 \theta^{(m)}}{\partial \eta^2} + \frac{1}{(\eta + \gamma)} \frac{\partial \theta^{(m)}}{\partial \eta} \right) + R_c, \tag{34}$$

$$\psi^{m+1} = -\frac{q}{2}, \frac{\partial \psi^{m+1}}{\partial \eta} = 1, w^{m+1} = 0, \theta^{(m+1)} = 0, \phi^{(m+1)} = 0, at \eta = h_1, \tag{35}$$

$$\psi^{(m+1)} = \frac{q}{2}, \frac{\partial \psi^{(m+1)}}{\partial \eta} = 1, w^{m+1} = 0, \theta^{(m+1)} = 1, \phi^{(m+1)} = 1, at \eta = h_2. \tag{36}$$

In the above expression, m is the iterative step index. It is emphasized that the above transmuted set of equations is linear in $\psi^{(m+1)}$.

(ii) This step deals with utilization of finite difference approximations of $\psi^{(m+1)}$, $w^{(m+1)}$, $\theta^{(m+1)}$, and $\phi^{(m+1)}$ along with their derivatives into Equations (36)–(38), which results in a linear set of algebraic equations at each iterative step.

(iii) The solution of the algebraic set of equation constructed above gives the numerical results for $\psi^{(m+1)}$, $w^{(m+1)}$, $\theta^{(m+1)}$, and $\phi^{(m+1)}$. In order to develop the iterative process, we need initial guesses for $\psi^{(m)}$, $w^{(m)}$, $\theta^{(m)}$, and $\phi^{(m)}$ as each cross section. The simulations are
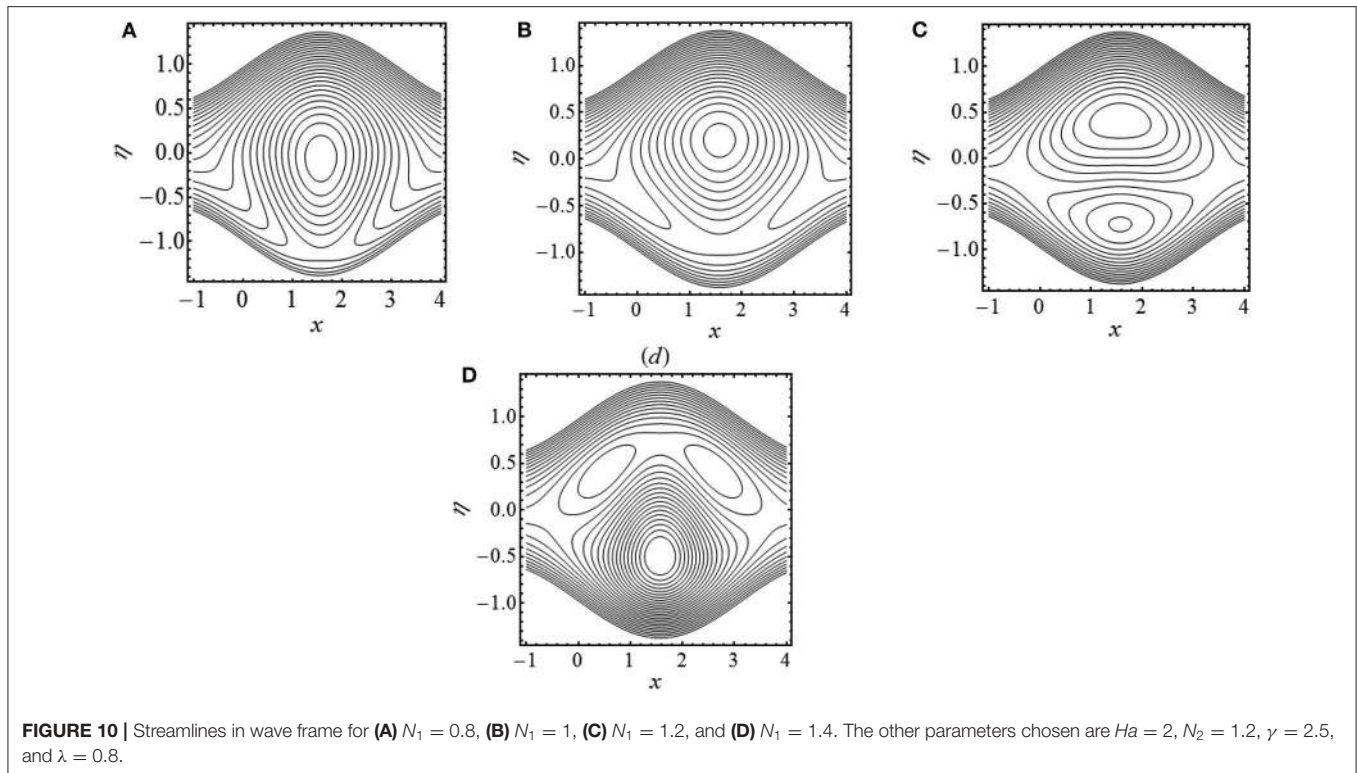
performed up to a desirable accuracy of solution. The fast convergence solution has been obtained by employing a successive under-relaxation technique. The values at of $\tilde{\psi}^{(m+1)}$, $\tilde{w}^{(m+1)}$, $\tilde{\theta}^{(m+1)}$ and $\tilde{\phi}^{(m+1)}$ at the $(m+1)$th iterative step are determined as

$$\psi^{(m+1)} = \psi^{(m)} + \tau (\tilde{\psi}^{(m+1)} - \psi^{(m)}),$$
$$w^{(m+1)} = w^{(m)} + \tau (\tilde{w}^{(m+1)} - w^{(m)}),$$
$$\theta^{(m+1)} = \theta^{(m)} + \tau (\tilde{\theta}^{(m+1)} - \theta^{(m)}),$$
$$\phi^{(m+1)} = \phi^{(m)} + \tau (\tilde{\phi}^{(m+1)} - \phi^{(m)}),$$

where τ denotes the under relaxation parameter. For excellent accuracy of the solution, the values of τ should be taken small. In
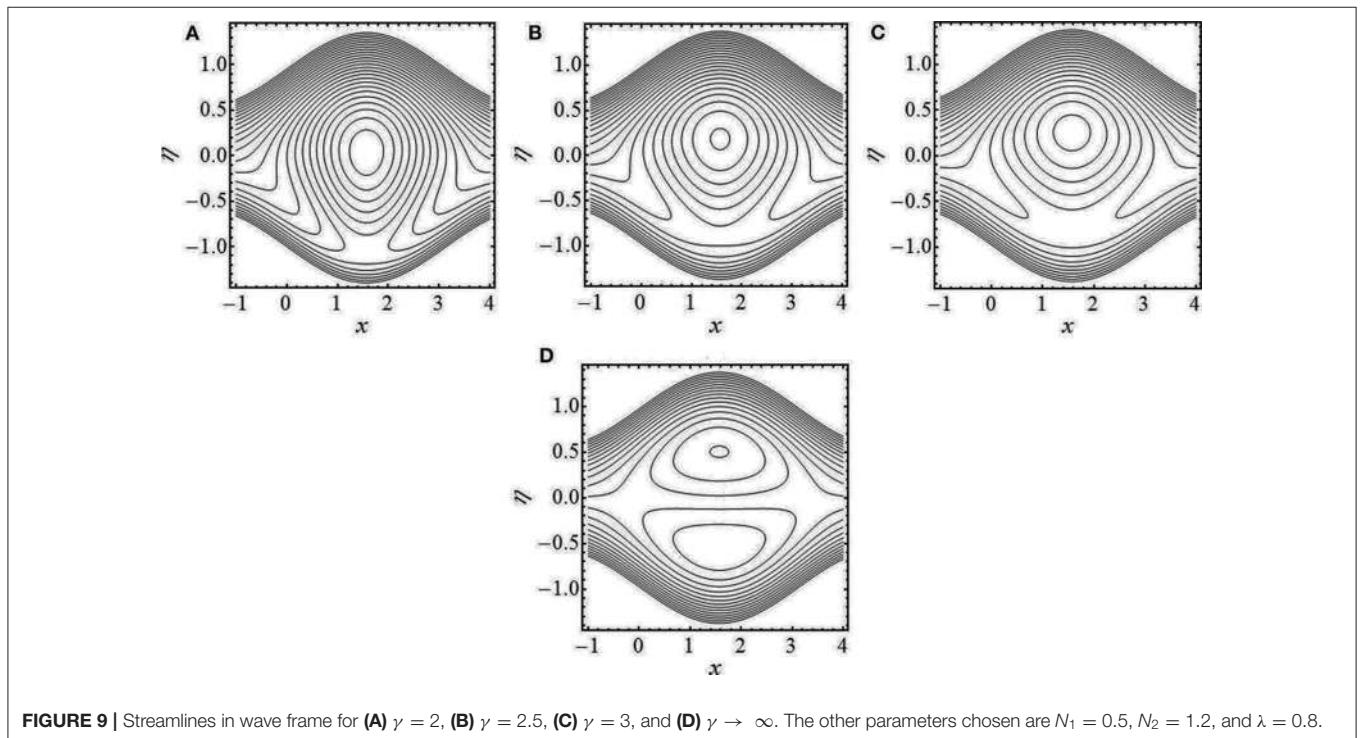
FIGURE 9 | Streamlines in wave frame for **(A)** $\gamma = 2$, **(B)** $\gamma = 2.5$, **(C)** $\gamma = 3$, and **(D)** $\gamma \to \infty$. The other parameters chosen are $N_1 = 0.5$, $N_2 = 1.2$, and $\lambda = 0.8$.

FIGURE 10 | Streamlines in wave frame for **(A)** $N_1 = 0.8$, **(B)** $N_1 = 1$, **(C)** $N_1 = 1.2$, and **(D)** $N_1 = 1.4$. The other parameters chosen are $Ha = 2$, $N_2 = 1.2$, $\gamma = 2.5$, and $\lambda = 0.8$.

the current situation, the convincing accuracy of 10^{-8} has been achieved for $\psi, w, \theta,$ and ϕ.

RESULTS AND DISCUSSION

To understand some momentous consequences of peristaltic aspects of flow features, pumping phenomenon, temperature distribution and trapping phenomenon for various values of coupling number (N_1), micropolar parameter (N_2), Brinkman number (Br), Hartmann number (Ha), and curvature parameter (γ), various graphs are provided in **Figures 2–5** with relevant consequences. The heat transfer characteristics at both wall surfaces are also visualized.

The effects of Hartmann number (Ha) on axial velocity $u(\eta)$ and micro rotation $w(\eta)$ are shown in **Figures 2A,B**. **Figure 2A** shows that $u(\eta)$ reached at peak level with a larger variation of Ha at the upper channel level in contrast to the lower wall channel. **Figure 2B** exhibits the effect of Hartmann number (Ha) on micro-rotation $w(\eta)$. In the lower channel region, $w(\eta)$ boosted up with the increment of Ha while its behavior is reversed in the upper part. The decrease in velocity with increasing Ha in the lower part of the channel is attributed to the resistive nature of the Lorentz force due to the applied magnetic field. In order to maintain the prescribed flux, the velocity attained a peak variation in the upper channel portion due to Ha. **Figure 3A** displays the effects of N_1 on axial velocity. The parameter N_1 reflects the vortex to the dynamic viscosity ratio of the fluid. In fact, it is a measure of which viscosity dominates the flow under consideration. Larger values of N_1 correspond to the situation in which vortex viscosity due to spinning motion of fluid particles dominates the flow, and as a result, axial velocity

$u(\eta)$ decreases in the upper channel region. In order to preserve the prescribed flow rate, the axial velocity $u(\eta)$ increases in the lower part of the channel with increasing N_1. **Figure 3B** shows an enhancement in the magnitude of micro-rotation component $w(\eta)$ with increasing N_1 in both parts of the channel. **Figure 4A** shows the impact of micropolar parameter (N_2) on $u(\eta)$. It is observed that $u(\eta)$ increases with increasing N_2 in the lower part of the channel. In contrast, $u(\eta)$ decreases with increasing (N_2) in the upper part of the channel. **Figure 4B** shows the effect of N_2 on $w(\eta)$. It is observed that $w(\eta)$ decreases in the lower portion of the channel while it increases in the upper portion with increasing N_2.

Figures 5A–C exhibit the effect of Hartmann number (Ha), coupling number (N_1), micropolar parameter (N_2), and curvature parameter (γ) on pressure rise per wavelength (Δp). The profiles of the pressure rise per wavelength for different values of Ha (Hartmann number) and coupling number (N_1) are shown in **Figures 5A,B**. It is observed that in pumping region $(\Theta > 0, \Delta p > 0)$, the pressure rise per wavelength increases with increasing Ha and N_1. The situation is different in the free pumping ($\Delta p = 0$) and co-pumping regions ($\Theta > 0, \Delta p < 0$). Here, Δp decreases by increasing Ha and N_1. **Figure 5C** shows the effects of micropolar parameter (N_2) on Δp. In the case of the micropolar parameter, an opposite trend is observed as seen in the figure.

The profiles of the temperature field for different values of the Brinkman number (Br), Hartmann number (Ha), coupling number (N_1), and micropolar parameter (N_2) are shown in **Figures 6A–D**. It is noted that θ increases over the entire cross section with each increase in $Br, N_1,$ and N_2. The increase in θ with increasing N_1 and N_2 is due to the retarding

effect of these parameters on velocity $u(\eta)$. The Brinkman number is a parameter which is the ratio of viscous heat to the heat transported by conduction. Larger values of Brinkman correspond to the scenario when heat generated due to viscous dissipation is dominant. In such situation, an enhanced temperature distribution in the channel has been justified. **Figure 6D** shows that θ decreases with increasing Ha. In order to determine how heat transfer coefficient z is altered for diverse values of Ha, N_1 and N_2 are displayed in **Figures 7A–C**. The behavior of z is clearly oscillating which is attributed to the oscillatory nature of the channel walls. A damping in amplitude of oscillations is observed with increasing Ha. The effects of Br (Brinkman number), R_c (rate of chemical reaction), Ha (Hartmann number), Sc (Schmidt number), and Sr (Soret number) on mass concentration ($\phi(\eta)$) can be observed in **Figures 8A–E**. It is observed that $\phi(\eta)$ is enhanced with increasing Br, R_c, Sc, and Sr. On the contrary, $\phi(\eta)$ turns down by varying Ha. The streamlines of flow inside the channel for different values of curvature parameter (γ) and coupling number (N_1) are shown in **Figures 9**, **10**. The objective is to investigate the trapping phenomenon. **Figure 9** shows the effect of the curvature parameter on streamlines. We noticed that for minimum values of γ, the fluid bolus has been concentrated in the upper channel region which is divided into symmetric parts due to increment in γ. The physical consequences of coupling number N_1 on streamlines are investigated by preparing **Figure 10**. Similar to earlier observations, the fluid bolus concentrated in the upper channel portion exists for lesser variation of coupling number ($N_1 = 0.8, 1$). The bolus has been ripped into two shapes as N_1 gets maximum values. However, the upper part is relatively bigger as compared to the lower part. The lower part of the bolus increases in size with increasing N_1 to 1.4. It is strongly anticipated that the upper part of the bolus vanishes with further increasing N_1 and the channel is only filled with a single bolus concentrated in the lower part.

CONCLUDING REMARKS

We have reported the transportation of the heat/mass phenomenon in the peristaltic study of micropolar liquid in a curved channel. The flow model is constructed via relevant equations which are treated numerically by employing the finite difference procedure. We summarized important observations from the current analysis in the following points:

❖ The axial velocity increases with impact of the micropolar parameter in the vicinity of the lower boundary whereas it shows an opposite behavior in the upper channel surface.
❖ The axial component of velocity attained the same trend due to variation of coupling number and Hartmann number.
❖ The pressure rise per wavelength increases with increasing Ha and N_1 in the pumping region.
❖ The temperature inside the channel follows an increasing trend with increasing N_1 and N_2. However, it shows a declining variation due to the impact of Ha.
❖ The concentration of fluid attained maximum variation with Br and R_c.
❖ The fluid bolus in the upper wall surface is split up into two parts as N_1 assigned leading numerical values.
❖ The streamline symmetry trend has been visualized when $\gamma \rightarrow \infty$.

DATA AVAILABILITY STATEMENT

The datasets generated for this study are available on request to the corresponding author.

AUTHOR CONTRIBUTIONS

All authors listed have made a substantial, direct and intellectual contribution to the work, and approved it for publication.

REFERENCES

1. Raju KK, Devanathan R. Peristaltic motion of non-Newtonian fluid, Part-I. *Rheol Acta.* (1972) **11**:170–8. doi: 10.1007/BF01993016
2. Mekheimer S. Non-linear peristaltic transport of magnetohydrodynamic flow in an inclined planar channel. *Arab J Sci Eng.* (2003) **28**:183–201.
3. Abd El Hakeem Abd El Naby, El Misery AEM, Abd El Kareem FM. Separation in the flow through peristaltic motion of a carreau fluid in uniform tube. *Phys A.* (2004) **343**:1–14. doi: 10.1016/j.physa.2004.05.072
4. Elshahed M, Haroun MH. Peristaltic transport of Johnson-Segalman fluid under effect of a magnetic field. *Math Prob Eng.* (2005) **6**:663–77. doi: 10.1155/MPE.2005.663
5. Abd El Hakeem Abd El Naby, El Misery AEM, Abd El Kareem FM. Effects of a magnetic field on trapping through peristaltic motion for generalized Newtonian fluid in channel. *Phys A.* (2006) **367**:79–92. doi: 10.1016/j.physa.2005.10.045
6. Hayat T, Ali N, Asghar S. Peristaltic motion of a Burger's fluid in a planar channel. *Appl Math Comput.* (2007) **186**:309–29. doi: 10.1016/j.amc.2006.07.098
7. Haroun MH. Effect of Deborah number and phase difference on peristaltic transport of a third order fluid in an asymmetric channel. *Commun Nonlin Sci Numerical Simul.* (2007) **12**:1464–80. doi: 10.1016/j.cnsns.2006.03.002

8. Wang Y, Hayat T, Ali N, Oberlack M. Magnetohydrodynamic peristaltic motion of a Sisko fluid in a symmetric or asymmetric channel. *Phys A.* (2008) **387**:347–62. doi: 10.1016/j.physa.2007.10.020
9. Ali N, Wang Y, Hayat T, Oberlack O. Slip effects on the peristaltic flow of a third grade fluid in a circular cylindrical tube. *J Appl Mech.* (2009) **76**:1–10. doi: 10.1115/1.2998761
10. Hayat T, Bibi S, Alsaadi F, Rafiq M. Peristaltic transport of Prandtl-Eyring liquid in a convectively heated curved channel. *PLoS ONE.* (2016) **11**:e0156995. doi: 10.1371/journal.pone.0156995
11. Maimona Rafiq, H.Yasmin, Hayat T, Alsaadi F. Effect of Hall and ion-slip on the peristaltic transport of nanofluid: a biomedical application. *Chin J Phys.* (2019) **60**:208–27. doi: 10.1016/j.cjph.2019.04.016
12. Ahmed B, Javed T. A study of full Navier-Stokes equations of peristaltic flow in a porous-saturated tube under the inducement of magnetic field: finite element analysis. *Chaos Solitons Fractals.* (2019) **125**:79–87. doi: 10.1016/j.chaos.2019.05.012
13. Asha SK, Sunitha G. Thermal radiation and Hall effects on peristaltic blood flow with double diffusion in the presence of nanoparticles. *Case Stud Therm Eng.* (2020) **17**:100560. doi: 10.1016/j.csite.2019.100560
14. Pietal AK. Flow past a sphere moving towards a wall in micropolar fluid. *J Theoret Appl Mech.* (1999) **37**:2.

15. Eringen AC. Some micro fluids. *Int J Eng Sci.* (1964) **2**:205–17. doi: 10.1016/0020-7225(64)90005-9

16. Eringen AC. *Microcontinuum Field Theories. II Fluent Media.* New York, NY: Springer Verlag (2001).

17. Ariman T, Turk MA, Sylvester N. Application of microcontinum fluid mechanics. *Int J Eng Sci.* (1974) **12**:273–93. doi: 10.1016/0020-7225(74)90059-7

18. Na TY, Pop I. Boundary-layer flow of a micropolar fluid due to a stretching wall. *Arch Appl Mech.* (1997) **67**:229–36. doi: 10.1007/s004190050113

19. Srinivasacharya D, Mishra M, Rao RA. Peristaltic pumping of a micropolar fluid in a tube. *Acta Mech.* (2003) **161**:165–78. doi: 10.1007/s00707-002-0993-y

20. Muthu P, Rathish Kumar BV, Chandra P. On the influence of wall properties in the peristaltic motion of micropolar fluid. *ANZIAM J.* (2003) **2**:245–60. doi: 10.1017/S1446181100013304

21. Lok YY, Amin N, Pop I. Steady mixed convection flow of a micropolar fluid near the stagnation point on a vertical surface. *Int J Numerical Methods Heat Fluid Flow.* (2005) **15**: 654–70. doi: 10.1108/09615530510613861

22. Hayat T, Ali N, Abbas Z. Peristaltic flow of a micropolar fluid in a channel with different wave forms. *Phys Lett A.* (2007) **370**:331–44. doi: 10.1016/j.physleta.2007.05.099

23. Ali N, Hayat T. Peristaltic flow of a micropolar fluid in an asymmetric channel. *Comp Math Appl.* (2008) **55**:589–608. doi: 10.1016/j.camwa.2007.06.003

24. Hayat T, Ali N. Effects of an endoscope on peristaltic flow of a micropolar fluid. *Math Comp Model.* (2008) **48**:721–33. doi: 10.1016/j.mcm.2007.11.004

25. Mekheimer Kh S. Peristaltic flow of a magneto-micropolar fluid: effect of induced magnetic field. *J Appl Math.* (2008) **23**:570825. doi: 10.1155/2008/570825

26. Ishak A, Nazar R, Pop I. Magnetohydrodynamic (MHD) flow of a micropolar fluid towards a stagnation point on a vertical surface. *Comput Math Appl.* (2008) **56**:3188–94. doi: 10.1016/j.camwa.2008.09.013

27. Kh. Mekheimer S, El Kot MA. The micropolar fluid model for blood flow through a tapered artery with a stenosis. *Acta Mech Sin.* (2008) **24**:637–44. doi: 10.1007/s10409-008-0185-7

28. Sajid M, Abbas Z, Hayat T. Homotopy analysis for boundary layer flow of a micropolar fluid through a porous channel. *Appl Math Model.* (2009) **33**:4120–5. doi: 10.1016/j.apm.2009.02.006

29. Ashraf M, Anwar Kamala M, Syeda KS. Numerical study of asymmetric laminar flow of micropolar fluids in a porous channel. *Comput Fluids.* (2009) **38**:1895–902. doi: 10.1016/j.compfluid.2009.04.009

30. Rashidi MM, Mohimanian Pour SA, Laraqi N. A semi-analytical solution of micropolar flow in a porous channel with mass injection by using differential transform method. *Nonlin Anal Model.* (2010) **15**:341–50. doi: 10.15388/NA.15.3.14329

31. Ali N. Sajid M. Javed T. Abbas Z. An analysis of peristaltic flow of a micropolar fluid in a curved channel. *Chin Phys Lett.* (2010) **28**:0147041–4. doi: 10.1088/0256-307X/28/1/014704

32. El–Dabe NT, Abou-zeid MY. The wall properties effect on peristaltic transport of micropolar non-Newtonian fluid with heat and mass transfer. *Math Prob Eng.* (2010) **2010**:898062. doi: 10.1155/2010/898062

33. Abd Elmaboud Y. Thermo micropolar fluid flow in a porous channel with peristalsis. *Porous Media J.* (2011) **14**:1033–45. doi: 10.1615/JPorMedia.v14.i11.70

34. Sui J, Zhao P, Cheng Z, Zheng L, Zhang X. A novel investigation of a micropolar fluid characterized by nonlinear constitutive diffusion model in boundary layer flow and heat transfer. *Phys Fluids.* (2017) **29**:023105. doi: 10.1063/1.4976642

35. Waqas H, Imran M, Khan SU, Shehzad SA, Meraj MA. Slip flow of Maxwell viscoelasticity-based micropolar nano particles with porous medium: a numerical study. *Appl Math Mech.* (2019) **40**:1255–68. doi: 10.1007/s10483-019-2518-9

36. Waqas H, Khan SU, Shehzad SA, Imran M. Radiative flow of Maxwell nanofluids containing gyrotactic microorganism and energy activation with convective Nield conditions. *Heat Transf Asian Res.* (2019) **48**:1663–87. doi: 10.1002/htj.21451

37. Ali N, Atif HM, Javed MA, Sajid M. A mathematical model of the calendered exiting thickness of micropolar sheet. *Polym Eng Sci.* (2018) **58**:327–34. doi: 10.1002/pen.24578

38. Ahmed R, Ali N, Javid K. Heat and mass transfer effects on the peristaltic flow of Sisko fluid in a curved channel. *Therm Sci.* (2017) **23**:331–45. doi: 10.2298/TSCI161018115A

39. Mekheimer Kh S, Hasona WM, Zaher AZ. Peristaltic blood flow with gold nanoparticles as a third grade nanofluid in catheter: application of cancer therapy. *Phys Lett A.* (2018) **382**:85–93. doi: 10.1016/j.physleta.2017.10.042

40. Abo-Elkhair R, Mekheimer Kh S, Zaher AZ. Electro-Magnetohydrodynamic oscillatory flow of a dielectric fluid through a porous medium with heat transfer: Brinkman model. *Bionanoscience.* (2018) **8** 596–608. doi: 10.1007/s12668-018-0515-6

41. Mekheimer Kh S, Zaher AZ, Abdellateef AI. Entropy hemodynamics particle-fluid suspension model through eccentric catheterization for time-variant stenotic arterial wall: Catheter injection. *Int J Geometric Methods Modern Phys.* (2019) **16**:1950164. doi: 10.1142/S0219887819501640

42. Mekheimer Kh S, Hassona WM, El-Shekhipy AA, Zaher AZ. Electrokinetics of dielectric non-newtonian bio fluids with heat transfer through a flexible channel: numerical study. *Comput Methods Sci Technol.* (2017) **23**:331–41. doi: 10.12921/cmst.2017.0000020

43. Nadeem S, Abbas N, Malik MY. Inspection of hybrid based nanofluid flow over a curved surface. *Comp Methods Prog Biomed.* (2020) **189**: 105193. doi: 10.1016/j.cmpb.2019.105193

44. Nadeem S, Abbas N, Elmasry Y, Malik MY. Numerical analysis of water based CNTs flow of micropolar fluid through rotating frame. *Comp Methods Prog Biomed.* (2019) **186**:105194. doi: 10.1016/j.cmpb.2019.105194

45. Abbas N, Malik MY, Nadeem S. Transportation of magnetized micropolar hybrid nanomaterial fluid flow over a Riga curface surface. *Comput Methods Prog Biomed.* (2020) **185**:105136. doi: 10.1016/j.cmpb.2019.105136

46. Sadaf H, Nadeem S. Fluid flow analysis of cilia beating in a curved channel in the presence of magnetic field and heat transfer. *Can J Phys.* (2020) **98**:191. doi: 10.1139/cjp-2018-0715

47. Nadeem S, Malik MY, Abbas N. Heat transfer of three-dimensional micropolar fluid on a Riga plate. *Can J Phys.* (2019) **98**:32–8. doi: 10.1139/cjp-2018-0973

48. Muhammad N, Nadeem S, Issakhov A. Finite volume method for mixed convection flow of Ag–ethylene glycol nanofluid flow in a cavity having thin central heater. *Phys A.* (2020) **537**:122738. doi: 10.1016/j.physa.2019.122738

49. Abbas N, Malik MY, Nadeem S. Stagnation flow of hybrid nanoparticles with MHD and slip effects. *Heat Trnasf Asian Res.* (2020) 180–96. doi: 10.1002/htj.21605

50. Hayat T, Khan WA, Abbas SZ, Nadeem S, Ahmad S. Impact of induced magnetic field on second-grade nanofluid flow past a convectively heated stretching sheet. *Appl Nanosci.* (2020). doi: 10.1007/s13204-019-01215-x. [Epub ahead of print].

51. B. Mallick J, Misra C. Peristaltic flow of Eyring-Powell nanofluid under the action of an electromagnetic field. *Eng Sci Technol Int J.* (2019) **22**:266–81. doi: 10.1016/j.jestch.2018.12.001

52. Ali N, Khan SU, Abbas Z. Hydromagnetic flow and heat transfer of a Jeffrey fluid over an oscillatory stretching surface. *Z Naturforsch.* (2015) **70**:567–76. doi: 10.1515/zna-2014-0273

53. Khan SU, Ali N, Abbas Z. Hydromagnetic flow and heat transfer over a porous oscillating stretching surface in a viscoelastic fluid with porous medium. *PLoS ONE.* (2015) **10**:e0144299. doi: 10.1371/journal.pone.0144299

54. Ali N, Khan SU, Abbas Z, Sajid M. Slip effects in the hydromagnetic flow of a viscoelastic fluid through porous medium over a porous oscillatory stretching sheet. *J Porous Media.* (2017) **20**:249–62. doi: 10.1615/JPorMedia.v20.i3.50

NOMENCLATURE

j	micro moment of inertia	$[ML^2]$	B^*	magnetic field	$[Wbm^{-2}]$
λ, λ'	amplitude ratio	$[m]$	T	temperature	$[K]$
ρ	density	$[kgm^{-3}]$	k^*	thermal conductivity	$[Wm^{-1}K^{-1}]$
Φ	dissipation function	$[kgm^{-1}s^{-3}]$	u_1, u_2	velocity component	$[ms^{-1}]$
C	mass concentration	$[kg]$	μ	viscosity parameter	$[kgm^{-1}s^{-1}]$
T_m	mean fluid temperature	$[K]$	c	wave speed	$[ms^{-1}]$
D	coefficient of mass diffusivity	$[m^2s^{-1}]$	$\alpha^*, \beta^*, \gamma,^*$	coefficient of angular velocity	$[MLT^{-1}]$